3D printing and pyrolysis of optical ZrO_2 nNanostructures by two-photon lithography: reduced shrinkage and crystallization mediated by nanoparticles seeds

Anne Desponds, Akos Banyasz, Denis Chateau, Azeddine Tellal, Amandine Venier, Sylvain Meille, Gilles Montagnac, Jerome Chevalier, Chantal Andraud, Patrice L. Baldeck, et al.

NANO · MICRO small
www.small-journal.com

3D Printing and Pyrolysis of Optical ZrO_2 Nanostructures by Two-Photon Lithography: Reduced Shrinkage and Crystallization Mediated by Nanoparticles Seeds

*Anne Desponds, Akos Banyasz, Denis Chateau, Azeddine Tellal, Amandine Venier, Sylvain Meille, Gilles Montagnac, Jérôme Chevalier, Chantal Andraud, Patrice L. Baldeck, and Stephane Parola**

Two-photon lithography is a potential route to produce high-resolution 3D ceramics. However, the large shrinkage due to the elimination of an important organic counterpart of the printed material during debinding/sintering remains a lock to further development of this technology. To limit this phenomenon, an original approach based on a composite resin incorporating 45 wt% ultrasmall (5 nm) zirconia stabilized nanoparticles into the zirconium acrylate precursor is proposed to process 3D zirconia microlattices and nanostructured optical surfaces. Interestingly, the nanoparticles are used both as seeds allowing control of the crystallographic phase formed during the calcination process and as structural stabilizing agent preventing important shrinkage of the printed ceramic. After 3D photolithography and pyrolysis, the weight and volume loss of the microstructures are drastically reduced as compared to similar systems processed with the reference resin without nanoparticles, and stable 3D microstructures of cubic zirconia are obtained with high spatial resolution. In the case of a patterned surface, the refractive index of 2.1 leads to a diffraction efficiency large enough to obtain microfocusing with linewidths of 0.1 µm, and the demonstration of a microlens array with a period as small as 0.8 µm.

1. Introduction

The set of techniques for manufacturing and production of micrometric-sized objects, often referred to as microfabrication, is key for many industries such as microelectronics, telecommunications, defense, microfluidics but also for biological applications. The techniques for making such objects are diverse, but traditionally based on linear patterning that involves the use of molds or masks.[1] Electron beam lithography (EBL) is mainly used for prototyping or making molds for replications.

Innovative processes for the direct 3D fabrication of sample with a complex shape at a sub-microscale are nowadays required. For the past 20 years, a manufacturing technique was developed, multiphotonic lithography, also called direct laser writing (DLW).[2] Direct laser writing can have very fast speeds (hundreds of m s^{-1}) for writing 2D structures on functional surfaces. This work has objectives to contribute to develop a massive parallelization process with millions of laser spots. Thus, direct laser writing could be used directly for the 3D nanostructuration of functional surfaces, in particular on detector windows (antifogging), CMOS wafers, biological surfaces. This technique, similar to some extent to stereolithography, allows the preparation of solid materials from liquid photosensitive resins by laser-induced photopolymerization. The polymerization is

A. Desponds, A. Banyasz, D. Chateau, A. Tellal, C. Andraud, P. L. Baldeck, S. Parola
Laboratoire de Chimie
CNRS UMR 5182
Ecole Normale Supérieure de Lyon
Université de Lyon 1
46 allée d'Italie, Lyon 69364, France
E-mail: stephane.parola@ens-lyon.fr

The ORCID identification number(s) for the author(s) of this article can be found under https://doi.org/10.1002/smll.202102486.

DOI: 10.1002/smll.202102486

A. Venier
Mathym SAS
22, rue des Aulnes, Champagne au Mont d'Or 69410, France
S. Meille, J. Chevalier
Univ Lyon, INSA Lyon, UCBL, CNRS, MATEIS
UMR 5510
7 avenue Jean Capelle, Villeurbanne 69621, France
G. Montagnac
Laboratoire de Géologie
CNRS UMR 5276
Ecole Normale Supérieure de Lyon
Université de Lyon 1
46 allée d'Italie, Lyon 69364, France

triggered by a photoinitiator, which is activated with the energy of a laser, the most common process being radical photopolymerization. The interest of the multiphoton strategy stands in its capacity to localize the polymerization reactions of the resin in three dimensions in a very precise way, at the focal point of a laser, allowing obtaining high-resolution 3D objects.[3]

This technique was first used to produce polymer-based objects based on acrylic resin[4,5] and hybrid sol-gel materials were then rapidly developed in order to provide better final mechanical properties.[6] Recent literature demonstrated that high-resolution inorganic SiCN or glassy carbon structures can be achieved[7,8] and that appropriating engineering the material and printing process sub-micrometer inorganic SiOC structures can be obtained.[9]

A large variety of photoresin formulations is compatible with the two-photon lithography, and can be adapted to the specifications required for the materials, such as mechanical[10] and optical properties[11] or biocompatibility.[12]

In the standard additive 3D printing, with feature control at a macroscopic scale, the usual photosensitive resins designed for 3D printing of ceramics are highly loaded in micron size particles. Then, the 3D printed objects are calcined to remove the organic matter, and to sinter the particles to obtain the ceramic object. However, the presence of microparticles induces a light-scattering effect in the resins, responsible for opacity. In this case, they cannot be used for the two-photon lithography that requires high transparency in the visible or near-infrared wavelengths.[13–17] To include inorganic component while keeping the optical properties, particle-less organic–inorganic resins were developed by including inorganic atoms in the molecular backbone or small inorganic clusters obtained via sol-gel reaction. This strategy was already used to produce inorganic-based materials structured via two-photon microfabrication, for example with titanium,[18–20] silica glass,[21] zinc,[22–24] and zirconium.[25–27] Among these materials, zirconia is particularly of interest because of its optical, mechanical, and electronic properties. The production of zirconia with controlled architecture at the subwavelength scale is of strong interest to process metasurfaces with subwavelength arrays of dielectric optical antennas. It has unique properties of high refractive index, transparency from UV to mid-infrared, and excellent resistance in harsh environments. In addition, it is a biocompatible material that can therefore be used in medical applications. To the best of our knowledge, no resin including only zirconia as inorganic matter has been reported so far for two-photon microfabrication.

Small particles with a diameter below 30 nm can avoid the scattering phenomena, and can be mixed into polymeric precursors while keeping the transparency. This strategy was used for producing high refractive index nanocomposites with other fabrication techniques.[28] The materials fabricated by two-photon lithography remain inorganic-organic composites with a low refractive index. Pyrolysis processes were implemented to reveal 3D microstructures of inorganic materials, including glass,[29] nickel,[30] zinc,[31] or silica-based materials.[32,33] However, in all cases, the loss of organic matter during the calcination process is important, leading to large volume loss and deformations of the printed materials, and altering the desired properties. The problems of volume shrinkage, shape fidelity, and mechanical behavior are of strong relevance in this topic, and strategies including theoretical aspects are developed along with that line.[34]

Herein, a first photoresin, acrylate-based, including zirconium and compatible with the two-photon lithography is studied. Commercial precursors with Zr atoms directly attached to acrylate function were used, in addition with a monomer and a photoinitiator. A second photoresin is proposed incorporating ultra-small zirconia nanoparticles (NPs) in the first acrylate-based zirconium photoresin. The control of the small size and of the surface state of the nanoparticles leads to a stable and light-scattering-free resin that can be further patterned with two-photon lithography. We describe the optimization of their formulations, and their characteristics after two-photon photopolymerization, i.e., structural resolution, mechanical response, and optical properties. We demonstrate the interest of NP-based resin in controlling the pyrolysis process by a comparison of 3D microstructures obtained by two-photon lithography, and debinding with the two resins. We present an example of optical application with subwavelength structures by the fabrication and characterization of a micro-lens array based on a highly diffractive microgrid with 0.1 μm linewidth.

2. Preparation of the Resins

In order to fulfill the criteria for two-photon microfabrication of ceramics, the resins need to show few key features. Of course, they require the presence of monomers and an appropriate photoinitiator to induce the crosslinking. It is necessary to incorporate the highest amount possible of metal (here zirconium) through a combination of zirconia nanoparticles loading and zirconium-based monomers. The particles need to be small enough to prevent any laser diffusion, which would lead to a loss in resolution. Viscosity should be adapted to allow control of reactive species diffusion and finally the overall stability (no particle aggregation, no parallel reaction) should be high enough to allow the process for a long period of time.

In that context, two resins were prepared, the reference one based on zirconium bromonorbornanelactone carboxylate triacrylate (PRM30), the second one by incorporation of zirconia ultrasmall functionalized nanoparticles.

PRM30 monomers have a large steric embedding, and triacrylate functionalities, which are favorable to obtain a stable cross-linking resin (see Supporting Information 1). Seven formulations were tested, with the addition of lower molecular weight cross-linkers to enhance the polymerization conversion, and to obtain a processable viscosity, i.e., DPHPA, DDA, and PETA (see Supporting Information 2 and Table S1, Supporting Information). The optimized resin was composed of 68 wt% PRM30, 28 wt% DPHPA, and 4 wt% of Michel ketone photoinitiator that are dissolved in about 10–20 wt% of 2-butanone after evaporation. The second resin was prepared from the reference formulation by replacing part of PRM30 with 45 wt% of zirconia nanoparticles. Thus, its concentration in zirconium is increased by a factor of 4.

Yttrium doped (8 mol%) ZrO_2 nanoparticles were prepared using a reported hydrothermal process.[35] The obtained nanoparticles, having a size of 5 ± 1 nm determined by TEM (see Supporting Information 3), were functionalized by aminohexanoic acid at their surface and dispersed in water (65 wt%, 25 vol%). They are crystalline and under tetragonal/cubic phase (evidenced by powder X-ray diffraction).

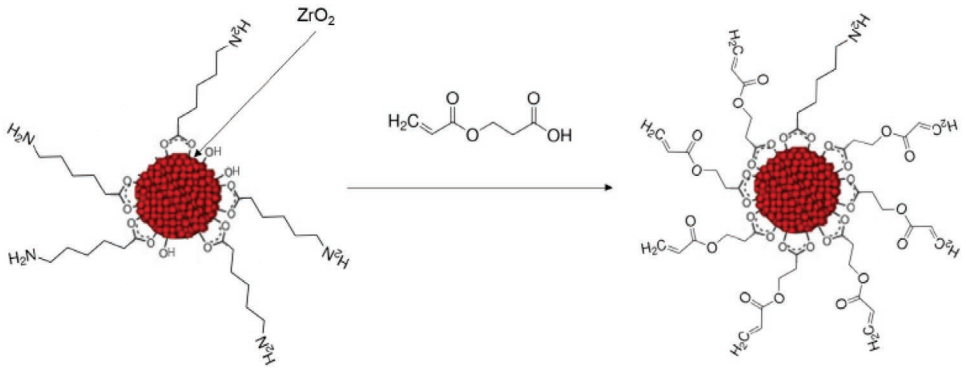

Figure 1. Illustration of the functionalization of the ZrO_2 particles.

The particles were then functionalized by 2-carboxyethyl acrylate to allow proper compatibility with zirconium bromonorbornanelactone carboxylate triacrylate during resin preparation (**Figure 1**). The surface functionalization of the particles is evidenced using ^{1}H-NMR and FT-IR). The shift of the ligand signals between the pure and the linked ones (See experimental section and Supporting Information 3), as well as the disappearance of the peak attributed to the proton of the carboxylic group indicates that the 2-carboxyethyl acrylate is linked to the nanoparticles.

Transparent and stable yellow suspensions of nanoparticles in the resin were obtained successfully (**Figure 2**). The presence of the nanoparticles leads to an increase of the refractive index from 1.6 for the reference acrylate-based resin to 1.8 for the NP-based resin, as determined by ellipsometry.

3. Radical Photopolymerization of the Resins

Two-photon lithography was performed at 532 nm (green laser). The UV–Vis absorption spectra of both resins diluted in ethanol are presented in **Figure 3**. They reveal no absorption and very low diffusion in the visible, in particular at 532 nm where the two-photon absorption occurs. The UV band at 350 nm corresponds to the Michler's ketone photoinitiator one-photon absorption.

The Michler's ketone allows the initiation of the polymerization reactions by the generation of radicals under UV light or laser excitation.[36] The acrylate functions bear typical C=C bonds that react to form C—C bonds during the polymerization process (**Figure 4**).

FTIR spectroscopy allowed monitoring the reaction through the peak attributed to the C=C bond at 1640 cm^{-1} (νCsp2-νCsp2) which decreases during polymerization. The ATR-FTIR spectra of both resins before and after an UV light exposure are presented in **Figure 5**. A close look at the elongation peak of the C=C vibration bond in the 1640 cm^{-1} area is also presented. As this band decreases after the UV exposure, it clearly evidences the ongoing polymerization, leading to the formation of the final solid material.

As expected with viscous cross-linking photoresins, the double bond conversions of different formulations increase with the concentration cross-linkers in the 20%-30% range (see Supporting Information 4). The resin that is highly loaded with zirconia nanoparticles has only 13% of double-bound conversion due to its low initial concentration of acrylate functions.

4. Two-Photon Lithography

The resins were processed using two-photon lithography. First of all, in order to determine their polymerization characteristics, simple lines from both resins were fabricated at different laser powers, and exposure times. They are well-defined with low polymerization thresholds and sub-wavelength resolutions

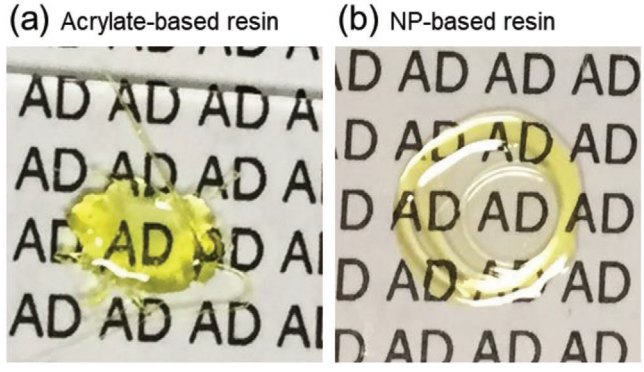

Figure 2. Transparent a) acrylate-based and b) NP-based (45 wt%, 15 vol%) resins on cover glasses.

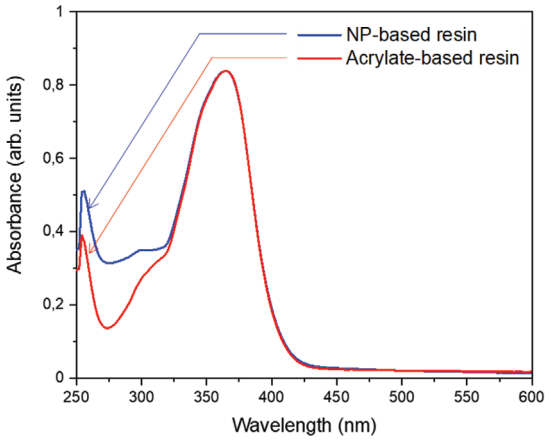

Figure 3. UV–vis absorption spectra of the two resins (diluted 10 000 times in ethanol).

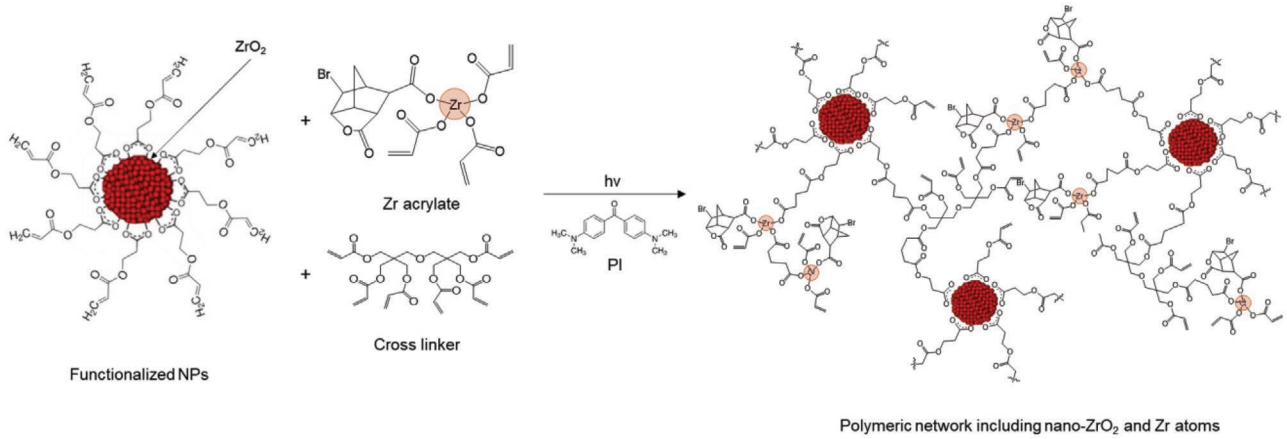

Figure 4. The copolymerization mechanism and the final hybrid structure in the case of the nanoparticles doped system.

when PETA or DPPHA cross-linkers are added (see Supporting Information 5). The line widths and heights have been measured in the suspended geometry between pillars by scanning electron microscopy (**Figure 6**). For an exposure time of 3 ms per voxel, threshold powers, minimal line widths and heights are in the ranges of 50–200 μW, 100–200 nm, and 200–400 nm, respectively (Figure 6 and Figure S5, Supporting Information). The fabrication power threshold of the nanoparticle-based resin is much larger than the acrylate-based resin, but their resolutions are similar close to their thresholds (Figure 6).

Then, the resins are processed using two-photon lithography towards more sophisticated 3D microstructures (**Figure 7**), such as a cube composed of 64 Archimedean tetradecahedrons (truncated octahedron), distributed in 4 layers of 4 × 4 ranks of polyhedrons. This geometric structure is arbitrarily chosen as a model for our study. However, the process can obviously be used to produce any type of other specific structures. The fabrication conditions are therefore different: as the laser often crosses over the same area, the exposition time is lowered to 1 ms and the fabrication thresholds are modified. The high-resolution microstructure is replicated several times and appears to be homogeneous and reproducible. For producing our geometrical structures, the conditions were optimized for each system based on the fabrication threshold and the

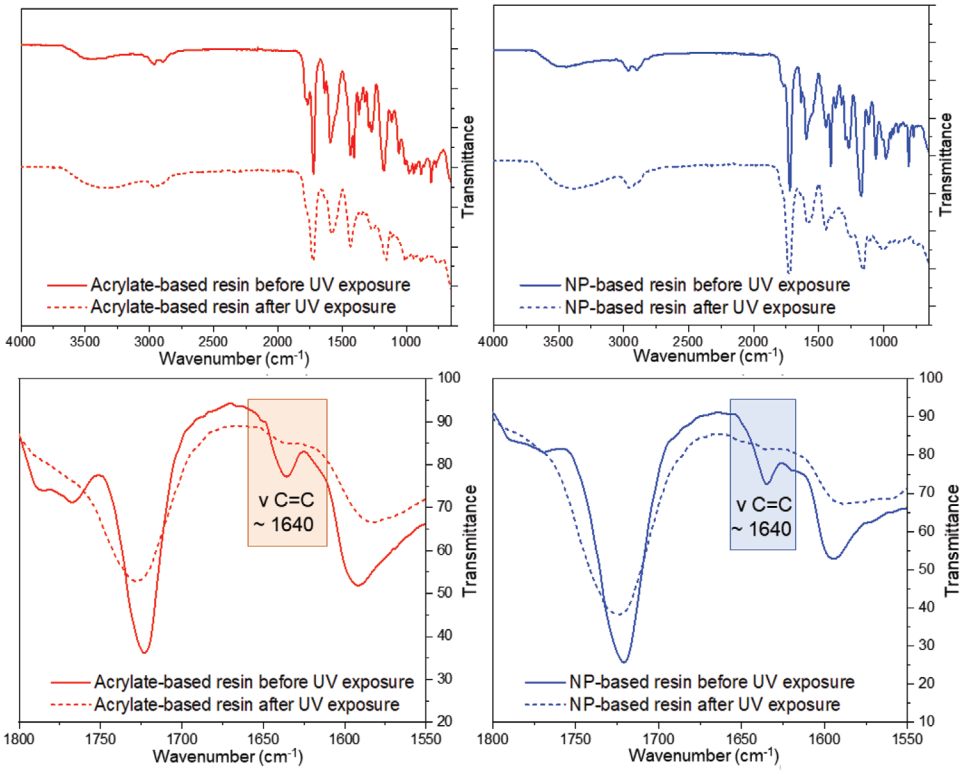

Figure 5. FTIR spectra of both resins before and after UV exposure in the range 650–4000 cm^{-1} and zooms on the C=C elongation at 1640 cm^{-1}.

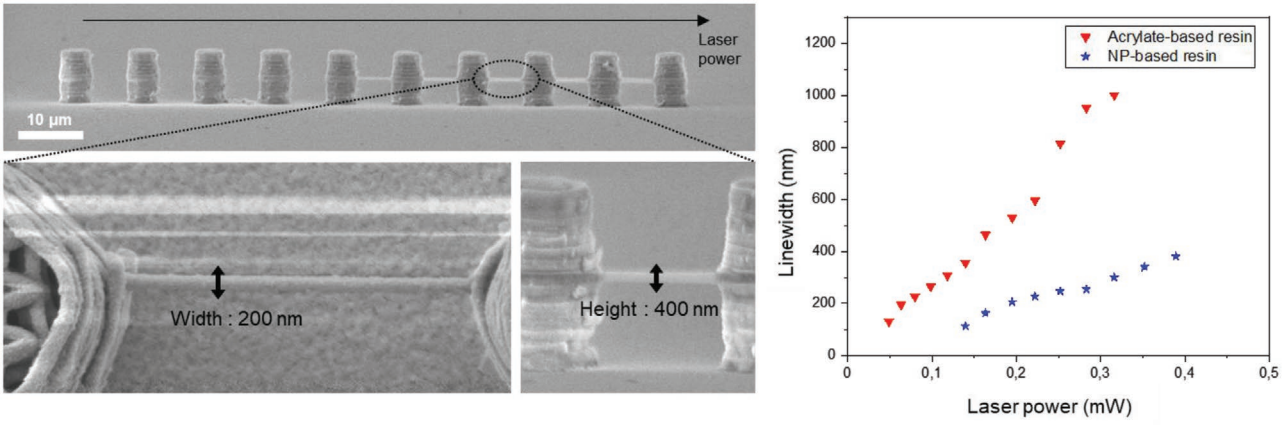

Figure 6. SEM of as prepared microfabricated suspended lines for the NPs based resin (left) and graphical presentation of obtained line widths versus laser powers (right).

resolution. The NP-based resin requires higher energy than the acrylate-based resin: typically, structures were fabricated at 100 µW from the acrylate-based resin, and at 200 µW from the NP-based resin. Similar high-resolution micro-objects were obtained in both cases such as observed in comparative Figure 7. This demonstrates that the presence of nanoparticles does not affect the process, the resolution, and the repeatability. Details of the resolution on the as-printed structures for the NPs based resin are visible on the higher magnification SEM images (**Figure 8**).

5. Formation of the Zirconia Phases

After the two-photon lithography process, the microfabricated objects are composed of an organic reticulated network containing zirconium atoms and of zirconia nanoparticles. Processing of the ceramics requires the removal of the organic parts and the sintering of the inorganic matter. To combine these two requirements, the systems undergo a thermal treatment to remove the organic matter by decomposition at high temperature and to sinter the particles. The evolution of

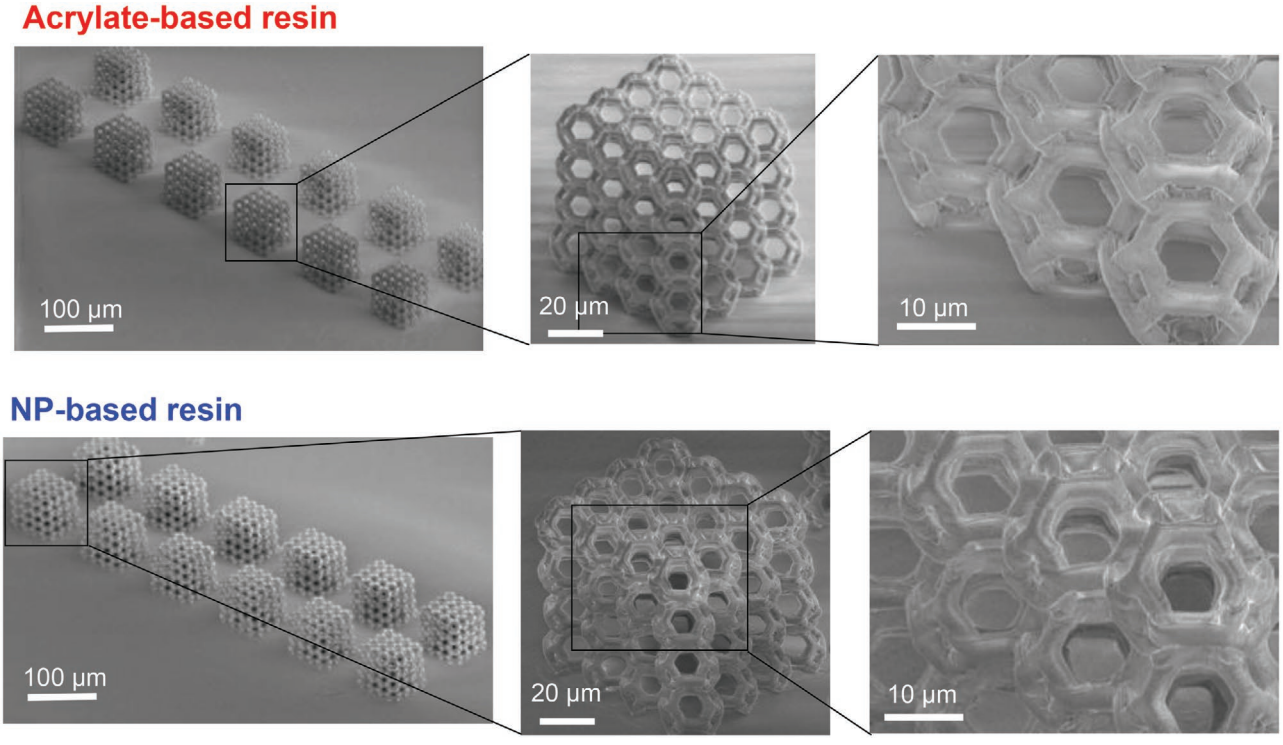

Figure 7. Geometrical structures and reproducibility of microcubes microfabricated by two-photon lithography with the acrylate-based resin and the NP-based resin (SEM observations).

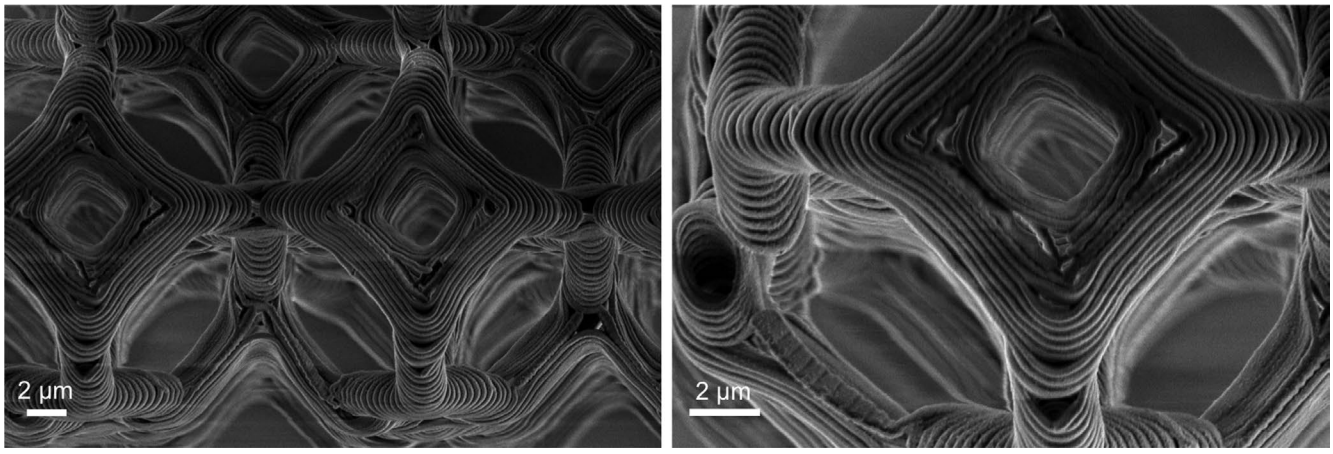

Figure 8. SEM observation showing the resolution of the printed objects for the NPs based resin.

the material formed during the pyrolysis is determined by X-ray diffraction (XRD) and micro-Raman as these analyses are complementary. XRD is performed on bulk material, obtained after the polymerization of the material under UV light whereas micro-Raman is performed directly on the microstructures obtained by the two-photon lithography process.

The XRD results are presented in **Figure 9**. Immediately after the formation of the polymerized material, it is possible to observe the presence of cubic zirconia nanoparticles in the NP-based system, whereas the XRD profile of the acrylate-based system obviously shows no crystalline material present in the polymerized material. When the temperature increases, the NP-based system crystallizes with growth of the seeds, as the diffraction peaks associated with cubic zirconia become thinner and more intense. The seeds thus play the role of templating agent and allow the propagation of the cubic phase to the whole material. Such behavior has been observed in the past and used for oriented crystallization of bulk pieces or films, for instance in the control of epitaxial crystallization of sol-gel derived materials such as pure perovskite structures,[37] or already in zirconia.[38] In this last example, sol-gel amorphous zirconia was deposited on single crystalline yttria-stabilized zirconia. Interestingly, in their case, ion-beam annealing at 300 °C provided cubic zirconia while thermal annealing at 900 °C led to a mixture of monoclinic (more than 50%) and cubic phases. They evidenced that the changes are related to kinetic differences between the two processes. This correlates well with our observations:

- when no particles are present at low temperature, cubic phase is obtained and a further increase of temperature induces phase transformation towards a monoclinic symmetry.
- however, when using zirconia nano-seeds, they act as a template and the cubic phase propagates to the matrix and the pure cubic phase remains stable even at high temperature.

In the case of the acrylate-based system, the XRD profile of the cubic phase appears at 500 °C, but the peaks are broad so it is not clear if they are well crystallized and if the formed phase is cubic or tetragonal. Then, a change of phase is observed from 700 °C to the monoclinic phase. Generally, the monoclinic phase is formed from 1000 °C but there is probably a size effect of the crystallites.[39] At 1100 °C, the mix of phases is definitively

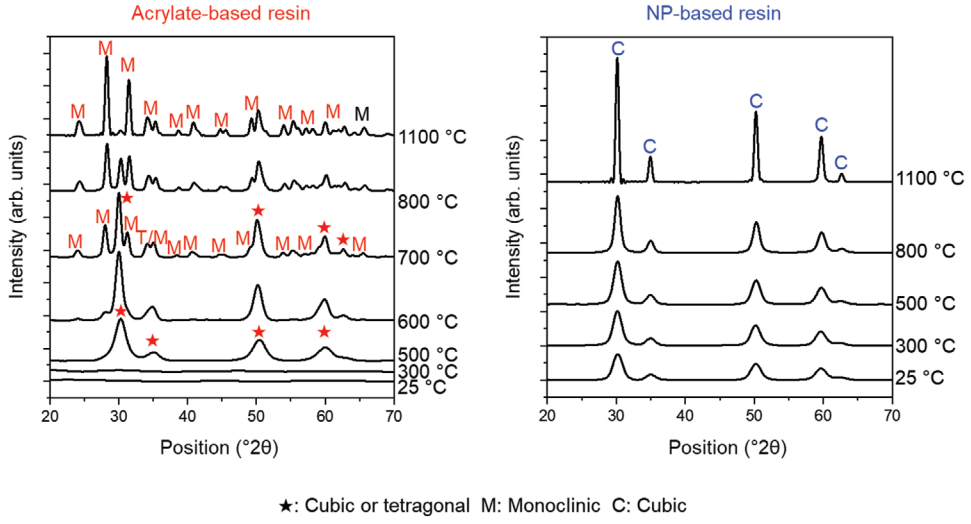

Figure 9. XRD profiles for the acrylate-based system and the NP-based system as a function of the temperature.

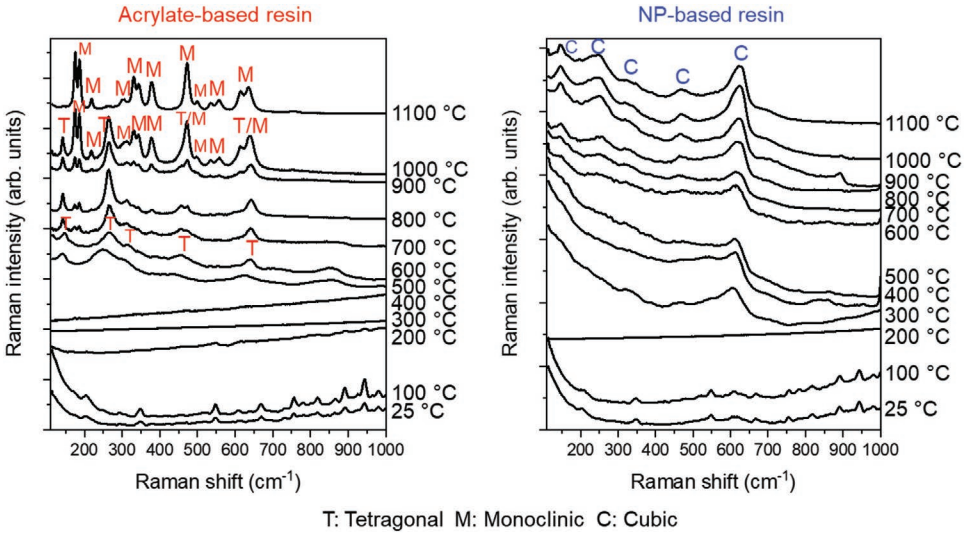

Figure 10. Raman spectra from microgrids fabricated with the acrylate-based resin and the NP-based resin as function of the temperature.

shifted to a unique monoclinic phase. The acrylates generally start to be calcined from 300 °C but the material remains still too amorphous to observe the formation of the ceramic phases. Considering these results, the pyrolysis temperature should be at least 500 °C to pretend producing a ceramic controlled at the submicron scale with this technique.

The micro-Raman results are presented in **Figure 10**. They are coherent with the XRD results, meaning that the phase formed does not depend on the polymerization process or on the structural properties (size, architecture) of the material. The spectra recorded at 25 °C and 100 °C are typical of the organic matter. At 200 °C the spectra evolve as the organic matter has started to decompose. Although the presence of the nanoparticles of zirconia is not visible at 25 °C because the signal is dominated by that of the organic parts, it is possible, in the case of NP based resins, to start to observe peaks typical of zirconia from 300 °C, corresponding to the loss of organic matter (Figure S8, Supporting Information). However, in the case of the acrylate-based resin, no inorganic signal is observed before 500 °C, which is also consistent with XRD measurements, because the system is still amorphous. For the NP-based system, the typical Raman signal of the cubic phase appears from 300 °C and this phase is retained when the temperature increases, as already noted with XRD. In the case of the acrylate-based system, the Raman signal of the tetragonal phase is observed from 500 °C. In this case, the Raman experiments allow concluding in favor of the formation of tetragonal phase rather than cubic at low temperature whereas the XRD was not clear because of the breadth of the peaks. The shift to the monoclinic phase at higher temperature from 700 °C is confirmed and the pure monoclinic phase is reached at 1100 °C. For both systems, the spectra show that the material becomes more crystalline with the temperature.

6. Reduced Shrinkage of the 3D Microstructure

The loss of organic matter causes inevitably a reduction in the size of the microstructures. Debinding is systematically associated with a very large shrinkage[30] and often with a loss of the shape,[31] appearing as an obstacle for a massive production. **Figure 11** shows a comparison of the volume loss because of the high-temperature thermal treatment for a similar microcube with both systems. According to the SEM pictures, the shrinkage of the acrylate-based system is much more important in comparison with the shrinkage of the NP-based system. However, in our experimental conditions, both systems, even the acrylate-based, are able to provide micro-objects without losing the initial shape.

On Figure 11, right, a comparison between two linear portions of the micro-object as function of the temperature is shown, for both resins. They correspond to the top and the bottom layer, as represented in the SEM picture of the acrylate-based system at 25 °C. The portion A corresponds to the length between the center of two tetradecahedrons located in the highest layer of the structure and the portion B corresponds to the length between the center of two tetradecahedrons located in the lowest layer of the structure. The results show that the shrinkage due to the loss of organics is identical for both portions, and homogenous, which allows to keep the shape of the object after thermal treatment. When preparing the 3D printing process, it becomes possible to simply consider the homogeneous reduction of size, which simplifies clearly the calculation for designing a ceramic micro-object with a complex shape. The NP-based system presents a reduced shrinkage which is a strong advantage over the acrylate-based system: the acrylate-based system presents a linear shrinkage of 53%, the NP-based system has only 19% of linear shrinkage between 20 and 1000 °C (Figure 11 right).

7. Mechanical Characterization

The objects were mechanically characterized in uniaxial compression using a nanoindenter equipped with a flat diamond tip (**Figure 12**). A target value of displacement is imposed on each sample until the fracture happens and the evolution of the applied load on the sample versus the displacement into the surface is recorded. It should be noted that despite the apparent

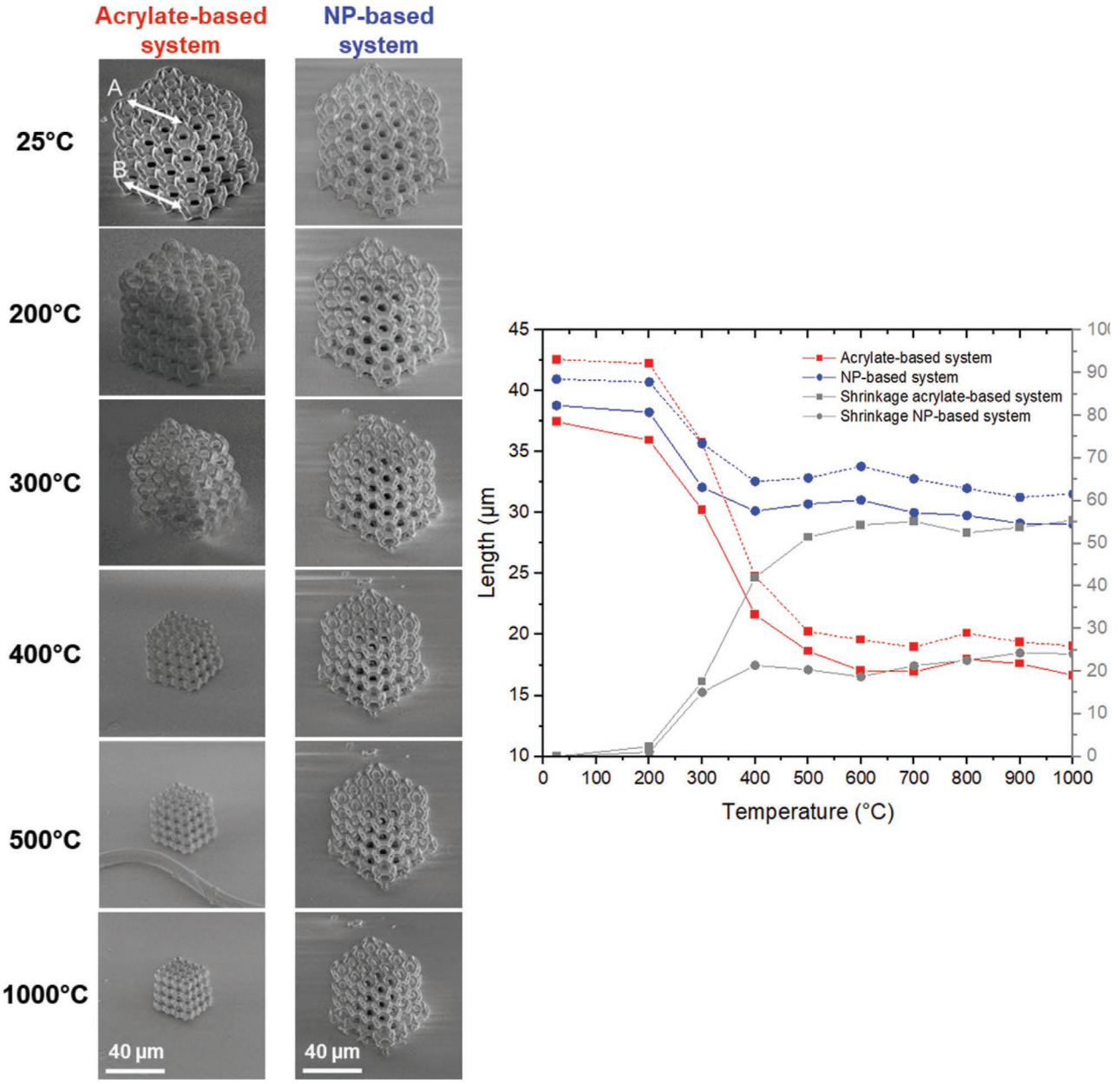

Figure 11. Left: SEM observations of the evolution of the micro-object during the pyrolysis as function of the temperature for the acrylate-based and the NP-based system. Right: Evolution of the length of two portions of the micro-object as function of the temperature for the acrylate-based and the NP-based system. Solid lines correspond to the portion A, the top layer, and dash lines correspond to the portion B, the bottom layer, as flagged on the first SEM picture.

reproducibility of the fabrication process, some defects in edges of the micro-objects, are present within the microstructures, due to the washing process and the handling of the substrate (Figure 12a and Figure 8). Additionally, the pyrolysis process induces the formation of microcracks within the calcined cubes (Figure 12b), these irregularities being fragilities area susceptible to cause early fracture under compression. Four tests are presented on the 3D objects as-printed with both resins and three tests on the 600 °C calcined 3D objects, again with both strategies. Corresponding stress-strain curves are presented in **Figure 13**. One sample corresponds to one compression test. All structures are brittle and tend to collapse at a certain stage of loading, as noted on the stress–strain curves by a sudden displacement jump at fracture load (flagged with two dashes on Figure 13). After the calcination, the structures have reduced in volume but as the loss of matter is homogeneous, the systems before and after the thermal treatment can be compared taking into account the difference of size. The apparent fracture stress σ_{max}, Young's modulus (E), and the compressive strain at fracture $\varepsilon_{fracture}$ are resumed in Supporting Information 6, Table S2) for the different modalities.

The mechanical properties of the printed zirconia are lower than the typical properties of the raw reference materials (strength of more than 1 GPa and Young's modulus of 200 GPa).

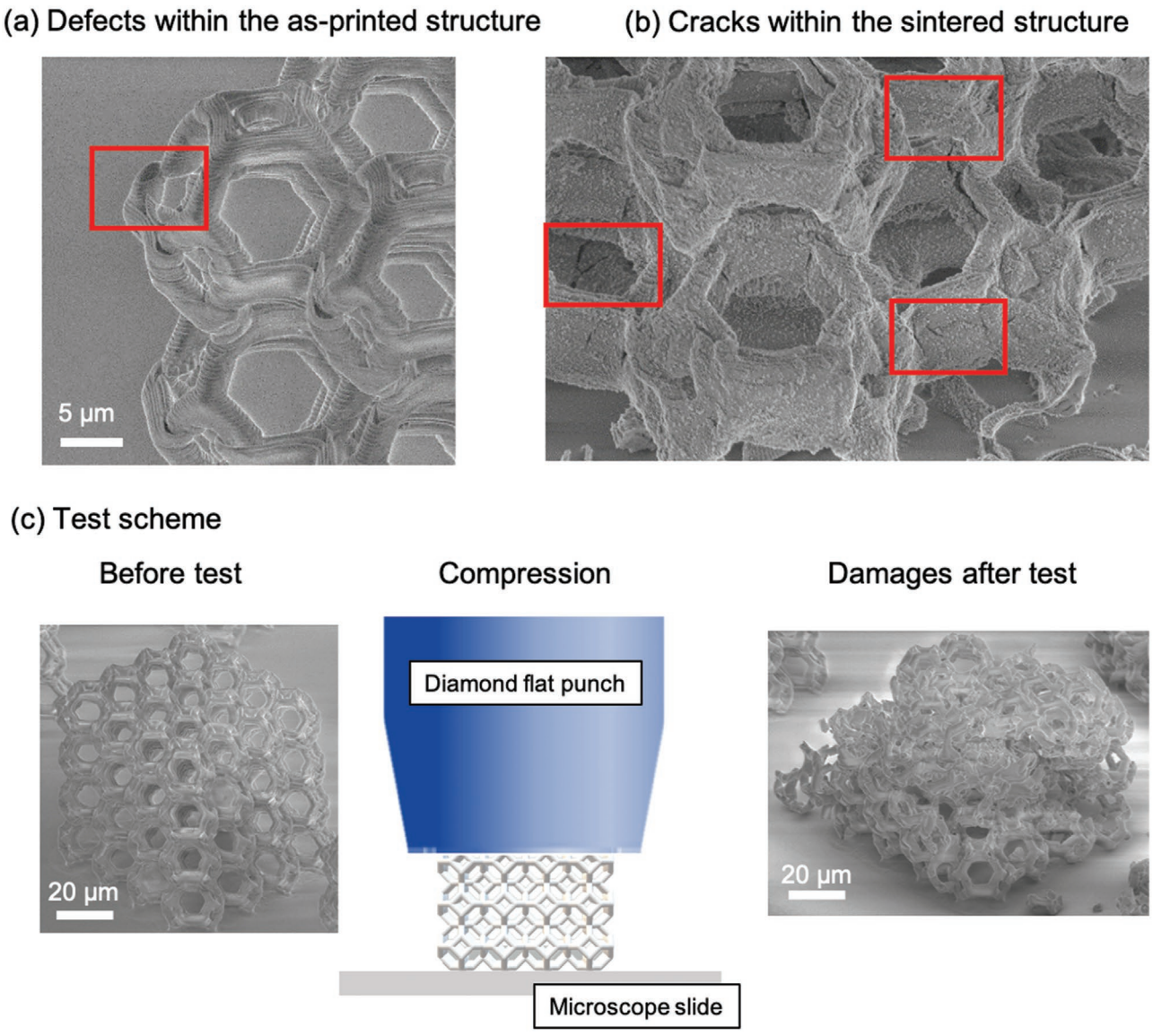

Figure 12. Illustration of the compression test with structures printed with the acrylate-based resin: a) Example of defects: as-printed cube and b) microcracks within a calcined cube. c) Test scheme and aspect of a microstructure before and after the test leading to the fracture of the sample.

This is obviously related to the high-volume fraction of voids in the architecture of the microstructures as in the two-photon fabrication field, previous studies show that the mechanical properties of the printed objects are widely depending on the material and on the architecture of the structure.[40,41] A rough estimation of the pore volume fraction based on an image analysis of the structures obtained gave an estimation of at least 80% of void in the as-printed cubes (Figure 8), which explains in part the apparent modest strength and Young's modulus of the structures obtained, while showing a strain to failure of several percent (which is much higher than for dense counterparts, mostly because of a lower stiffness).

For the as-printed materials, the acrylate-based resin shows superior properties as compared with the NP-based one, both in terms of fracture stress and Young's modulus. One could expect that the addition of ceramic nanoparticles would lead to an increase in Young's modulus that is not found here. Indeed, the rule of mixture in properties commonly used in composite materials is often found not to be valid for organic nanocomposites.[42] This can be related to the small size of reinforcements, that implies a large interfacial surface between polymer and nanoparticles, then a notable modification of crosslinking in the organic phase as compared to the neat polymer, as illustrated in Figure 4. The acrylate-based resin also contains PRM30 that may favor polymerization conversion and helping the optimization of final properties.

After pyrolysis, the mechanical properties are lower in terms of strength and quite similar in terms of Young's modulus, while one would expect an improvement of both due to the conversion towards a ceramic system during sintering. Figure 12b shows micro-cracks present in the sintered materials, which may account for this decrease in strength. The difference between the two process routes is still retained on both strengths while Young's modulus does not differ significantly.

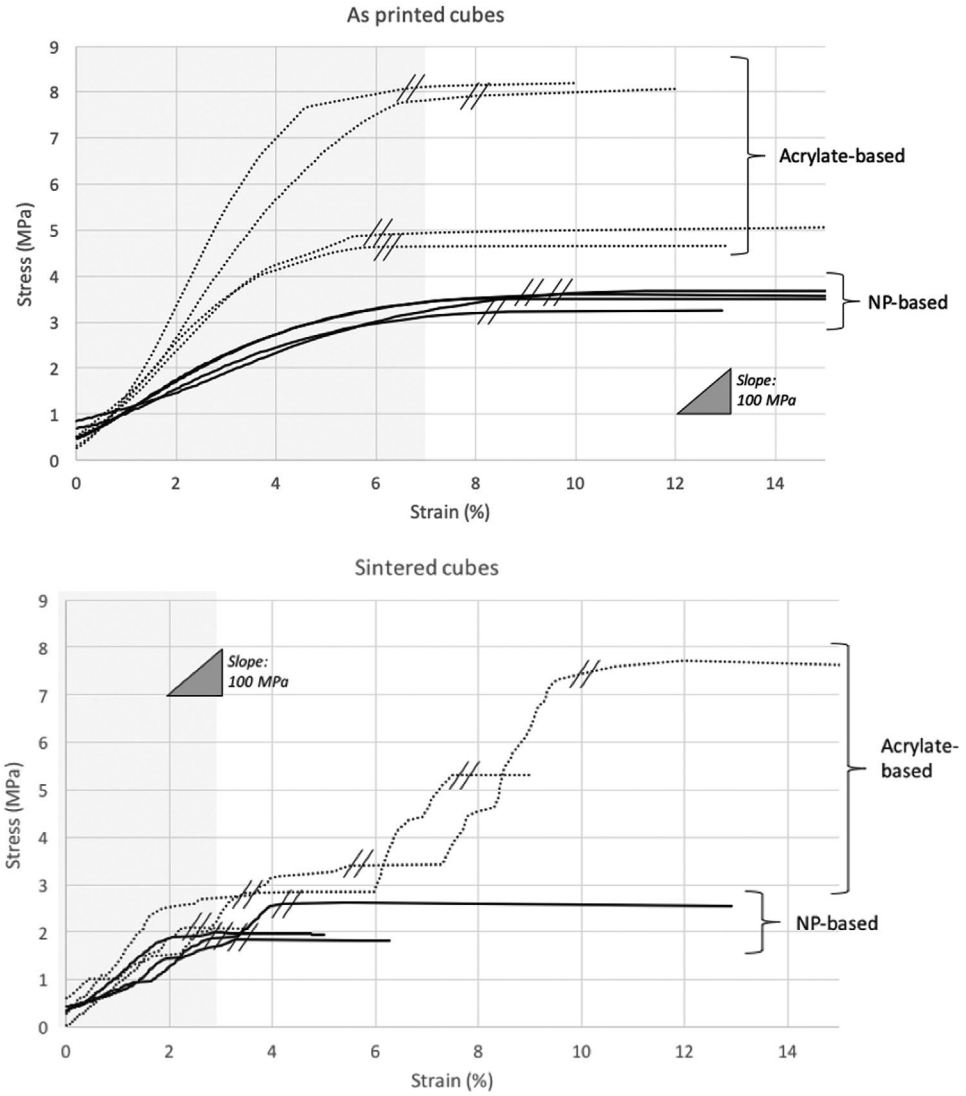

Figure 13. Stress–strain curves of the 3D as-printed cubes (top) and the 3D calcined (at 600 °C) cubes (bottom), with both systems. Dashes show the fracture events, recorded by a sudden displacement of the indentation punch.

Two parameters may account for this: the presence of defects and the influence of the zirconia phases. A larger density of defects in NP-based systems was not evident and the volume variation during thermal treatment was lower for this system. Moreover, a smaller scattering is noted in the mechanical properties noted in NP-based systems as compared with acrylate-based. Thus, the effect of zirconia crystallography may account for these final slightly lower mechanical properties of the NP-based system at the end of the process. It is to note also that if the maximum stress was higher in the acrylate-based printed structures in average, the values were more dispersed and the onset of damage in all cases was quite similar to the NP-based system (around 2–3 MPa, for a strain of 2–3%).

Finally, concerning the mechanical properties, the NP-based cubes tend to show smaller but less scattered fracture stresses as compared to the acrylate-based cubes, in all conditions (as printed and after sintering), certainly thanks to a better shape fidelity. This may be important in practical terms and suggests that the structures obtained with the NP-based systems, being less deformed especially after sintering are likely to be more robust in terms of properties. Overall, after the calcination, the zirconia phase formed is different but the mechanical properties are quite close between the two systems. Similar microstructures made of ZnO show a compressive strain at fracture of 3% after calcination,[31] which matches our results when considering the onset of damage. This is interesting since it shows that open architectures of that kind can deform to several percent before the collapse. Limiting the presence of micro-cracks and playing with phase content and phase transformation toughening may be one major goal to improve the strength of such structures.

8. Diffractive Optical Nanostructures with High Refractive Index and Resistant ZrO_2

Recently, there has been a surge on the manufacturing of optical surfaces based on patterns of subwavelength nanostructures

that are designed to obtain established and new optical properties with flat surfaces. The nanostructured patterns are designed (refractive index, size, geometry, orientation, and arrangement) to obtain the amplitude and phase distributions needed for the targeted applications including focusing, polarization control, and hologram generation.[43–45] For example, they have been used to realize ultrathin lightweight metalenses that have achromatic corrections, and high numerical apertures, leading to low-cost and easy to integrate lens components, weightless light concentrators, and miniature optical cameras.[46] Such optical metasurfaces have been originally made with silicon nanostructures easily to manufacture with microelectronics technologies. For applications in the visible regime, TiO_2, GaN, and c-Si are often selected for their high refractive index and low absorption.[47] A wide variety of fabrication techniques have been developed to fabricate 2D optical metasurfaces. Two-photon polymerization emerges as the unique alternative technique to fabricate nanostructures with 3D geometries leading to more sophisticated optical properties.[48] In this part, we report on the first fabrication of ZrO_2 nanolines that can be used to build 3D optical metasurfaces with excellent mechanical, chemical, and temperature resistances in harsh environments. ZrO_2 is transparent from UV to mid-infrared, and has high refractive index (2.1 to 2.3) in the visible.[49]

Regarding the obtained refractive indexes for our materials (measured on films), treated under UV light to simulate the photon excitation, the values are consistent with expectations. The materials prepared without the particles present a refractive index of 1.6 as prepared, which increased to 2.0 after annealing at 1000 °C. When the resin contains zirconia nanoparticles, the as prepared film shows an index of 1.8 increasing to 2.1 after annealing at 1000 °C.

An example of microgrid, elaborated from the nanoparticle-based resin, with a period of 1 µm is shown in **Figure 14**. It has been obtained with 1 mW average power, and 2 ms exposure time. After pyrolysis, the linewidth and the line height are about 100 and 500 nm, respectively.

Previously, we have used the two-photon polymerization of acrylates to demonstrate the fabrication of microlens arrays based on the diffraction of microgrids.[50] We obtained periods as small as 1.2 µm, that are needed for the continuous trend of downsizing the pixel size of CMOS sensors.[51] Due to the low refractive index of 1.5, the optimized line widths and heights, for high diffraction efficiency, were 0.4 and 0.8 µm, respectively. The minimum array period was limited by the wavelength-size spacing that was needed for the light propagation. In the following, we show that the high refractive index of cubic ZrO_2 leads to a diffraction efficiency large enough to obtain microfocusing with x4 smaller linewidths of 0.1 µm opening the possibility to obtain array periods smaller than 1.2 µm. **Figure 15** shows the experimental 3D microfocusing patterns obtained with a microgrid array of 0.8 µm spacing. The focal size is about 400 nm (full width half maximum). This x2 reduction of light spreading in a sensor pixel would be sufficient to eliminate the pixel cross-talk during the electronic detection. All the experimental and simulations details are described in ref. [50].

9. Conclusion

In this study, we have developed a photosensitive resin including nanoparticles, limiting the loss of matter during the debinding. The small size of the used zirconia nanoparticles makes this resin transparent and compatible with two-photon lithography, and the possibility of obtaining smooth and resolved microobjects. The NP-based resin offers three advantages, i) the shrinkage due to the loss of organic matter is strongly reduced compared to the acrylate system, ii) the zirconia seeds allows the growth of microceramic in the pure and stable cubic phase, and iii) the presence of nanoparticles offers also a strong improvement in the optical properties of the microfabricated objects, even without any thermal treatment.

The development of resins including nanoparticles for the two-photon lithography permits to provide stable 2D/3D highly resolved microstructures in zirconia in a simple manner. Similar strategy can be objectively imagined for wide range of material compositions. The possible limitations are on one hand related to the availability of colloidal crystalline NPs of the

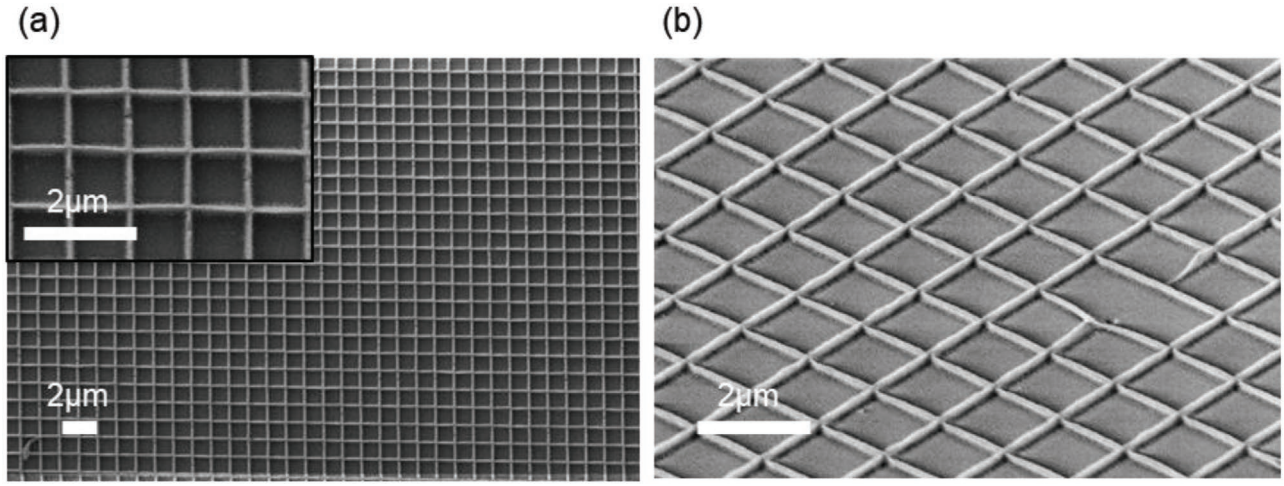

Figure 14. Pyrolyzed microgrid with a period of 1 µm: a) view from the top b) view with 45° tilt.

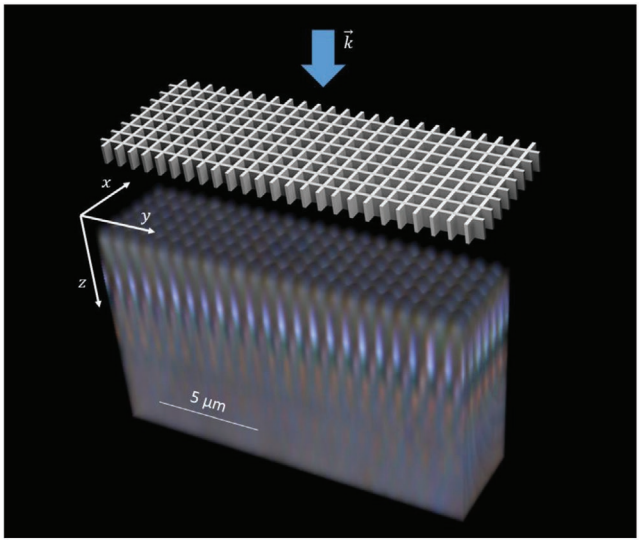

Figure 15. Experimental 3D microfocusing pattern for a pyrolyzed ZrO_2 microgrid with a period of 0.8 µm.

material, with sufficient small size and stability to prevent diffusion and aggregation; and on the other hand to the control of the reactivity of the metal's molecular precursors incorporated to the resin.

ZrO_2 microlenses were successfully produced. The focusing efficiency of this microlens array with 0.8 µm spacing demonstrates the potential to manufacture optical metasurfaces with sub-wavelength nanostructures based on cubic ZrO_2, and its unique resistance properties. Using two-photon polymerization will also allow the design and fabrication of more complex nanostructures, and optical properties with 3D geometries.

10. Experimental Section

Chemicals: Zirconium bromonorbornanelactone carboxylate triacrylate, 2-carboxyethyl acrylate (contains 900–1100 ppm MEHQ as inhibitor) and dipentaerythritol penta-/hexa-acrylate (contains < 650 ppm MEHQ as inhibitor) were purchased from Sigma Aldrich and used without further purification. 2-butanone (99+%, extra pure) and 1-propanol (99+%, extra pure) were purchased from Acros Organics and used without further purification. 4,4'-Bis(dimethylamino)-benzophenone (for synthesis), also known as Michler's ketone, was purchased from Merck and was recrystallized from toluene. Commercial 5 nm tetragonal/cubic yttrium (8 mol%) stabilized zirconia nanoparticles (5 nm) were provided by the company Mathym, they are sold dispersed in water (67 wt%).

Acrylate-Based Resin: In a 12 mL amber glass vial, 1 g of zirconium bromonorbornanelactone carboxylate triacrylate was slowly added to 7 mL of 2-butanone and strongly stirred for 24 h on a magnetic stirrer. This solution of zirconium acrylate was centrifuged at 6000 rpm for 2 min and filtered. In a 3 mL amber glass vial, 13.8 mg of Michler's ketone was dissolved in 0.7 mL of 2-butanone and 0.5 mL of 1-propanol under magnetic agitation. Then, in this 3 mL amber vial, 0.08 g of dipentaerythritol penta-/hexa-acrylate, dissolved in 50 µL of 2-butanone, and 1.53 g of the first solution of zirconium acrylate were added. The preparation was mixed on a magnetic stirrer for 5 min. About 80% of the solvent was removed by letting the vial evaporated under a fume hood for 24 h. To ensure a long-time stability, the formulation was stored in the fridge (4 °C). A yellow translucent viscous resin was obtained.

Particles Functionalization: In a centrifugation tube, 0.25 g of zirconia nanoparticles were dissolved in 4 mL of distilled water and 0.42 g of 2-carboxyethyl acrylate were added. The mixture was shaken vigorously and placed in a domestic microwave (700W) for 10 seconds. After a washing in ethanol, the particles were dispersed in 220 µL of 2-butanone.

^{1}H-RMN: About 5 mg of pure 2-carboxyethyl acrylate were diluted in about 500 µL of acetone D6 and about 5 mg of functionalized particles (under powder form) are diluted in about 500 µL of $CDCl_3$. They were analyzed with a Bruker spectrometer (300 MHz, 5mm probe BBFO ^{1}H-X).

NMR (300 MHz, $CDCl_3$): The pure 2-carboxyethyl acrylate shows six peaks: 10.22 (s, 1H, carboxylic function), 6.46 (m, 1H, acrylate function), 6.13 (m, 1H, acrylate function), 5.90 (m, 1H, acrylate function), 4.42 (m, 2H), 2.71 (m, 2H). The treated nanoparticles show 5 peaks: 6.32 (m, 1H, acrylate function), 6.03 (m, 1H, acrylate function), 5.78 (d, J = 9 Hz, 1H, acrylate function), 4.31 (m, 2H), 2.61 (m, 2H).

NP-Based Resin: In a 12 mL amber glass vial, 1 g of zirconium bromonorbornanelactone carboxylate triacrylate was slowly added to 7 mL of 2-butanone and strongly stirred for 24 h on a magnetic stirrer. This solution of zirconium acrylate was centrifuged at 6000 rpm for 2 min and filtered. In a 3 mL amber glass vial, 5 mg of Michler's ketone were weighted. Then, in this 3 mL amber vial, 0.1 g of functionalized zirconia nanoparticles suspension (53 wt%), 0.2 g of the solution of zirconium acrylate and 0.05 g of dipentaerythritol penta-/hexa-acrylate were added. The preparation was mixed on a magnetic stirrer for 5 min. About 80% of the solvent was removed by letting the vial evaporated under fume hood for 24h. To ensure a long-time stability, the formulation was stored in the fridge (4 °C). A yellow translucent viscous resin was obtained.

Spectroscopic Ellipsometry: Both resins (10 µL) were spin-coated (6000 rpm/30 s; Acceleration 1000 rpm s^{-1}) onto a degreased silicon substrate and exposed to UV light (20 µW cm^{-2}) for 15 min. The systems were analyzed by an ellipsometer UVISEL Horiba, in a range of wavelength of 400–800 nm. The refractive indexes were determined by regressive calculation using the Cauchy dispersion model.

Microfabrication by Two-Photon Lithography: The microfabrication setup (Microlight 3D) is based on an inverted microscope. The irradiation source is a Q-switched, frequency-doubled Nd-YAG laser (532 nm, 12 kHz, 560 ps) focused by a microscope objective (Oil 100x/NA = 1.4, Zeiss) into the sample. During the microfabrication, the focused laser spot is scanned through the trajectory defining the 3D microstructure to be printed, which is realized by varying the sample position by a piezo stage with respect to the focal spot. The microfabrication parameters such as 3D trajectory, laser power, exposure time all are controlled by a dedicated software. For the microfabrication of structures with the acrylate-based resin, the exposure time was 1ms and the power was 100 µW. For the microfabrication of structures with the NP-based resin, the exposure time was 1ms and the power was 200 µW.

A quartz cover slide (24 × 24 × 0.17-0.18 mm) has undergone a defatting process: the slide was placed in a first ultrasonic bath of KOH solution (5%) for 15 min, then a second ultrasonic bath of acetone for 15 min and finally the slide was dried under isopropanol vapor. A drop of the resin was deposited onto this quartz cover slide substrate. The fabrication was carried out on the surface of the quartz slide. After the printing, the sample was developed in acetone for 5 min to remove the excess of unreacted resin.

UV–Vis Spectroscopy: The solvent of the resin, 2-butanone, absorbs in the UV range so the resins were diluted in ethanol (10 000 times) to perform the measurement. The analyses were conducted using a spectrophotometer from PerkinElmer (Lambda750), in plastic tank. The UV-Vis spectra were recorded from 250 to 650 cm^{-1} and are presented without any post-treatment.

IR Spectroscopy: Two drops of 5 µL of both resins were deposited onto a glass slide. The first drop was directly analyzed and the second drop was exposed to UV light (20 µW cm^{-2}) for 15 min, in order to polymerize the material, then the second drop was analyzed. The analyses were conducted using a FTIR spectrometer equipped with an ATR device from PerkinElmer (Spectrum65). The glass slides were placed on the device

and their signals were subtracted during the record of a background. The FTIR spectra were performed from 650 to 4000 cm^{-1} and are presented without any posttreatment.

SEM Observations: The microstructures were observed with a SEM (Supra55VP, Zeiss) at a beam of 3 kV, through a secondary electron detector. When possible, the microstructures were sputtered with a 5 nm layer of platinum using a high vacuum coater (EM ACE600, Leica), in this case the SEM beam was 10 kV.

Pyrolysis Process: The microfabricated structures were calcined directly on a quartz slide placed in an alumina crucible. The heating was conducted by a muffle furnace (Thermolyne FB1300, Thermo Scientific) without particular airflow regulation. A temperature ramp of 3 °C min^{-1} was applied up to the temperature, then it was maintained for 60 min before allowing the oven to cool down to room temperature without any particular control. The temperature was varied from 25 °C, meaning that the microstructures was as fabricated (no heating process performed) to 1100 °C, the limit temperature that the quartz slide could tolerate.

XRD Experiments on the Bulk Materials: The resins were prepared as described below and were exposed to UV light (20 μW cm^{-2}) for 1 h, until a solid is formed. The materials were crushed in fine powders in a mortar. They were calcined as described in the pyrolysis process below and diffractograms were recorded after the heating treatment at 25 °C, 300 °C, 500 °C, 800 °C, 1100 °C. For the acrylate-based resin, diffractograms for a pyrolysis of 600 °C and 700 °C were also performed to observe well the phase change. The diffractograms were performed from 10° to 80° but they are presented here from 20° to 70° as the structural information is mainly located in this range. The diffractograms were post-treated to adjust the background and to smooth the lines.

Micro-Raman Analysis on the Microfabricated Material: Simple grids of 50 μm were fabricated by two-photon lithography. They were calcined as described in the pyrolysis process below and the Raman spectra were recorded after the heating treatment at 25 °C, 100 °C, 200 °C, 300 °C, 400 °C, 500 °C, 600 °C, 700 °C, 800 °C, 900 °C, 1000 °C, and 1100 °C.

The micro-Raman instrument allows analyzing directly the chemistry of the surface of the microstructures, with a laser through a microscope objective focused on a precise location of the micro-object, without further preparation. The micro Raman analyses were conducted with a Horiba LabRamn HR evolution spectrometer. In backscattering geometry, the excitation laser (532 nm) was focused and the Raman diffusion was collected through the same objective (x100/0.9 Olympus). The probe size of the device is lower than 1 μm that is adapted to a precise localization on the microstructure, so Raman spectra are obtained at this precise position. Different locations were analyzed and it appears that the microstructures are homogenous. For this reason, the spectra were not processed, they are presented as measured. The spectra were conducted with 10 scans during 5 s, in the range 110 to 1000 cm^{-1} as the structural information is localized in this area.

Mechanical Characterization: The structures were printed on microscope slides with the acrylate resin by two-photon lithography. They were attached to a metal holder with extra strong glue. The nanoindenter is a G200 (Agilent, USA). The sticks were placed on the motorized stage of the instrument. The area to be indented is located and selected under a microscope, then the motorized stage brings it under a 100 μm flat punch in diamond. After the detection of the contact point by an increase of the stiffness, the tip sinks into the cube to perform the compression test. The value of the displacement into the surface is managed by integrated software. The fracture stress was calculated as the maximal load reached divided by the section of the object and the deformation at failure as the ratio of the height variation at fracture on the initial height. Stiffness was measured as the maximum slope in the initial part of the load–displacement curve. Young's modulus was calculated from stiffness during loading or during unloading phase, considering the apparent dimensions of the cube. Samples dimensions were measured from SEM pictures.

Imaging of the Microfocusing Patterns: The experimental diffraction patterns were recorded by 3D wide-field transmission imaging using an inverted microscope (Zeiss Axivert 200) with an oil immersion objective (Zeiss Plan Apochromat, × 100 NA = 1.4). The incident illumination, from a collimated nonpolarized halogen white light, was spatially narrowed (diameter < 1 mm) to improve its spatial coherence. The 3D diffraction patterns were obtained by taking z-stacks of color images at different depths (0.5 μm-spacing) inside the glass substrate with a CMOS camera based on Sony's 2.3 MP sensor IMX174 (1936 × 1216 px).

Supporting Information

Supporting Information is available from the Wiley Online Library or from the author.

Acknowledgements

This project was received funding from the European's Union Horizon 2020 research and innovation program under grant agreement n° 780278. PHENOmenon project is an initiative of the Photonics Public-Private Partnership. The dissemination of results herein reflects only the author's view and the European Commission is not responsible for any use that may be made of the information it contains. The authors are also grateful to the Raman facility in Lyon (France) supported by the Institut National des Sciences de l'Univers (INSU), and to the LABEX Lyon Institute of Origins (ANR-10-LABX-0066) of the Université de Lyon for its financial support within the program "Investissements d'Avenir" (ANR-11-IDEX-0007) of the French government operated by the National Research Agency (ANR).

Conflict of Interest

The authors declare no conflict of interest.

Data Availability Statement

Research data are not shared.

Keywords

3D printing, nanoparticles, subwavelength nanostructures, two-photon lithography, zirconia

Received: April 28, 2021
Revised: July 13, 2021
Published online: September 14, 2021

[1] M. J. Madou, *Fundamentals of Microfabrication: The Science of Miniaturization*, 2nd ed., CRC Press, Boca Raton, FL **2002**.
[2] T. Baldacchini, *Three-Dimensional Microfabrication Using Two-Photon Polymerization: Fundamentals, Technology, and Applications*, William Andrew, Norwich, NY **2015**.
[3] H.-B. Sun, S. Kawata, in *Advances in Polymer Science*, (Eds: N. Fatkullin, T. Ikehara, H. Jinnai, S. Kawata, R. Kimmich, T. Nishi, Y. Nishikawa, H.-B. Sun), Springer, Berlin **2004**, pp. 169–273.
[4] S. Maruo, O. Nakamura, S. Kawata, *Opt. Lett.* **1997**, *22*, 132.
[5] A. Ostendorf, B. Chichkov, *Photonics Spectra* **2006**, *40*, 72.
[6] M. Farsari, B. Chichkov, *Nat. Photonics* **2009**, *3*, 450.
[7] J. Bauer, A. Schroer, R. Schwaiger, O. Kraft, *Nat. Mater.* **2016**, *15*, 438.
[8] T. A. Pham, D.-P. Kim, T.-W. Lim, S.-H. Park, K.-S. Lee, *Adv. Funct. Mater.* **2006**,*16*, 1235.
[9] L. Brigo, J. E. M. Schmidt, A. Gandin, N. Michieli, P. Colombo, G. Brusatin, *Adv. Sci.* **2018**, *5*, 1800937.

[10] E. D. Lemma, F. Rizzi, T. Dattoma, B. Spagnolo, L. Sileo, A. Qualtieri, M. De Vittorio, F. Pisanello, *IEEE Trans. Nanotechnol.* **2017**, *16*, 23.
[11] J. Serbin, A. Ovsianikov, B. Chichkov, *Opt. Express* **2004**, *12*, 5221.
[12] A. Ovsianikov, B. Chichkov, P. Mente, N. A. Monteiro-Riviere, A. Doraiswamy, R. J. Narayan, *Int. J. Appl. Ceram. Technol.* **2007**, *4*, 22.
[13] J. Z. Manapat, Q. Chen, P. Ye, R. C. Advincula, *Macromol. Mater. Eng.* **2017**, *302*, 1600553.
[14] M. Layani, X. Wang, S. Magdassi, *Adv. Mater.* **2018**, *30*, 1706344.
[15] J. W. Halloran, *Annu. Rev. Mater. Res.* **2016**, *46*, 19.
[16] R. D. Farahani, M. Dubé, D. Therriault, *Adv. Mater.* **2016**, *28*, 5794.
[17] A. Selimis, V. Mironov, M. Farsari, *Microelectron. Eng.* **2015**, *132*, 83.
[18] I. Sakellari, A. Gaidukeviciute, A. Giakoumaki, D. Gray, C. Fotakis, M. Farsari, M. Vamvakaki, C. Reinhardt, A. Ovsianikov, B. N. Chichkov, *Appl. Phys. A* **2010**, *100*, 359.
[19] A. Vyatskikh, A. Kudo, S. Delalande, J. R. Greer, *Mater. Today Commun.* **2018**, *15*, 288.
[20] S. Passinger, M. S. M. Saifullah, C. Reinhardt, K. R. V. Subramanian, B. N. Chichkov, M. E. Welland, *Adv. Mater.* **2007**, *19*, 1218.
[21] I. Cooperstein, E. Shukrun, O. Press, A. Kamyshny, S. Magdassi, *ACS Appl. Mater. Interfaces* **2018**, *10*, 18879.
[22] C.-C. Yeh, H.-C. Liu, W. Heni, D. Berling, H.-W. Zan, O. Soppera, *J. Mater. Chem. C* **2017**, *5*, 2611.
[23] C.-C. Yeh, H.-C. Liu, M.-Y. Chuang, J. Denzer, D. Berling, H.-W. Zan, O. Soppera, *Adv. Mater. Interfaces* **2016**, *3*, 1600373.
[24] L. Guo, H. Xia, H.-T. Fan, Y.-L. Zhang, Q.-D. Chen, T. Zhang, H.-B. Sun, *Opt. Lett.* **2010**, *35*, 1695.
[25] A. Ovsianikov, A. Gaidukeviciute, B. N. Chichkov, M. Oubaha, B. D. Maccraith, I. Sakellari, A. Giakoumaki, D. Gray, M. Vamvakaki, M. Farsari, C. Fotakis, *Lasers Chem.* **2008**, *2008*, 493059.
[26] A. Ovsianikov, J. Viertl, B. Chichkov, M. Oubaha, B. MacCraith, I. Sakellari, A. Giakoumaki, D. Gray, M. Vamvakaki, M. Farsari, C. Fotakis, *ACS Nano* **2008**, *2*, 2257.
[27] B. Bhuian, R. J. Winfield, S. O'Brien, G. M. Crean, *Appl. Surf. Sci.* **2006**, *252*, 4845.
[28] N. Nakayama, T. Hayashi, *Composites, Part A* **2007**, *38*, 1996.
[29] F. Kotz, K. Arnold, W. Bauer, D. Schild, N. Keller, K. Sachsenheimer, T. M. Nargang, C. Richter, D. Helmer, B. E. Rapp, *Nature* **2017**, *544*, 337.
[30] A. Vyatskikh, S. Delalande, A. Kudo, X. Zhang, C. M. Portela, J. R. Greer, *Nat. Commun.* **2018**, *9*, 593.
[31] D. W. Yee, M. L. Lifson, B. W. Edwards, J. R. Greer, *Adv. Mater.* **2019**, *31*, 1901345.
[32] O. Dufaud, S. Corbel, *Rapid Prototyping J.* **2002**, *8*, 83.
[33] D. Gailevičius, V. Padolskytė, L. Mikoliūnaitė, S. Šakirzanovas, S. Juodkazis, M. Malinauskas, *Nanoscale Horiz.* **2019**, *4*, 647.
[34] B. Cardenas-Benitez, C. Eschenbaum, D. Mager, J. G. Korvink, M. J. Madou, U. Lemmer, I. D. Leon, S. O. Martinez-Chapa, *Microsyst. Nanoeng.* **2019**, *5*, 38.
[35] A. Venier, E. Camposilvan, WO2020109477 (A1), 2019.
[36] R. O. Kan, *Organic Photochemistry*, McGraw-Hill, New York, NY **1966**.
[37] T. Tani, D. A. Payne, *J. Am. Chem. Soc.* **1994**, *77*, 1242.
[38] N. Yu, *Philos. Mag. Lett.* **2010**, *73*, 1996.
[39] P. Bouvier, E. Djurado, C. Ritter, A. J. Dianoux, G. Lucazeau, *Int. J. Inorg. Mater.* **2001**, *3*, 647.
[40] L. R. Meza, A. J. Zelhofer, N. Clarke, A. J. Mateos, D. M. Kochmann, J. R. Greer, *Proc. Natl. Acad. Sci. USA* **2015**, *112*, 11502.
[41] J. Bauer, S. Hengsbach, I. Tesari, R. Schwaiger, O. Kraft, *Proc. Natl. Acad. Sci. USA* **2014**, *111*, 2453.
[42] Y. Song, Q. Zheng, *Prog. Mater. Sci.* **2016**, *84*, 1.
[43] W. T. Chen, A. Y. Zhu, F. Capasso, *Nat. Rev. Mater.* **2020**, *5*, 604.
[44] S. Chen, W. Liu, Z. Li, H. Cheng, J. Tian, *Adv. Mater.* **2020**, *32*, 1805912.
[45] J. Scheuer, *ACS Photonics* **2020**, *7*, 1323.
[46] H. Liang, A. Martins, B. H. V. Borges, J. Zhou, E. R. Martins, J. Li, T. F. Krauss, *Optica* **2019**, *6*, 1461.
[47] S. M. Choudhury, D. Wang, K. Chaudhuri, C. DeVault, A. V. Kildishev, A. Boltasseva, V. M. Shalaev, *Nanophotonics* **2018**, *7*, 959.
[48] V. C. Su, C. H. Chu, G. Sun, D. P. Tsai, *Opt. Express* **2018**, *26*, 13148.
[49] I. Bodurov, T. Yovcheva, S. Sainov, *J. Phys.: Conf. Ser.* **2014**, *558*, 012062.
[50] A. Tellal, O. Ziane, S. Jradi, O. Stephan, P. L. Baldeck, *Nanophotonics* **2019**, *8*, 1051.
[51] A. Tellal, O. Ziane, P. L. Baldeck, *Chin. Opt. Lett.* **2019**, *17*, 082201.